

Large-scale EM Analysis of the *Drosophila* Antennal Lobe with Automatically Computed Synapse Point Clouds

Ting Zhao, Shin-ya Takemura, Gary B. Huang,
Jane Anne Horne, William T. Katz,
Kazunori Shinomiya, Louis K. Scheffer,
Ian A. Meinertzhagen, Patricia K. Rivlin, Stephen M. Plaza

September 22, 2018

Abstract

The promise of extracting connectomes and performing useful analysis on large electron microscopy (EM) datasets has been an elusive dream for many years. Tracing in even the smallest portions of neuropil requires copious human annotation, the rate-limiting step for generating a connectome. While a combination of improved imaging and automatic segmentation will lead to the analysis of increasingly large volumes, machines still fail to reach the quality of human tracers. Unfortunately, small errors in image segmentation can lead to catastrophic distortions of the connectome.

In this paper, to analyze very large datasets, we explore different mechanisms that are less sensitive to errors in automation. Namely, we advocate and deploy extensive synapse detection on the entire antennal lobe (AL) neuropil in the brain of the fruit fly *Drosophila*, a region much larger than any densely annotated to date. The resulting synapse point cloud produced is invaluable for determining compartment boundaries in the AL and choosing specific regions for subsequent analysis. We introduce our methodology in this paper for region selection and show both manual and automatic synapse annotation results. Finally, we note the correspondence between image datasets obtained using the synaptic marker, antibody nc82, and our datasets enabling registration between light and EM image modalities.

1 Introduction

EM data provide a definitive way to identify synapses from the apposition of pre- and postsynaptic organelles. Figure 1 shows synapses in *Drosophila* from the locations of presynaptic organelles called T-bars, which are T-shaped when cut in cross section. Each synapse is clearly observed to have a presynaptic density and often a characteristic polyad of postsynaptic partners. Advances in machine

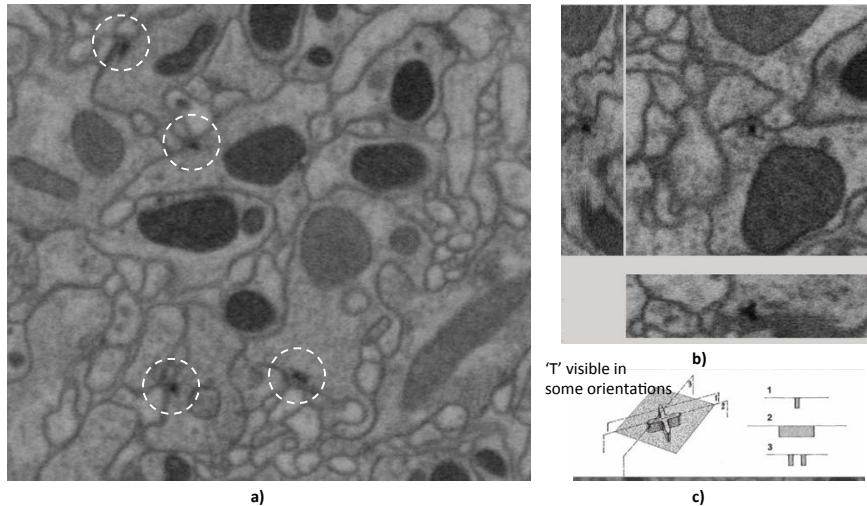


Figure 1: **Examples of synapses in EM dataset.** a) The dashed circles highlight a few synapses in the antennal lobe of *Drosophila*. They are often characterized by a T shaped structure (called a T-bar) and each T-bar has multiple post-synaptic partners. b) The same T-bar in three orthogonal views reveals that it has the form of a tiny table, comprising a platform surmounting a cruciform pedestal. c) Cartoon depicting the structure of the T-bar (adapted from Trujillo-Cenóz, 1969 [18]).

learning algorithms that use these characteristics [8, 12] could enable large-scale, automated identification of synaptic contacts, which could eliminate the need for time-consuming manual annotation [16]. Note that while synapse prediction promises to be an important contributor to connectomics, the task of tracing neurons is still laborious [22, 7].

In this paper, we introduce high-level applications of synapse prediction in EM that require minimal manual effort. In particular, we exploit the fact that identifying synapses in EM can be used to generate a *synapse point cloud* that is the high-resolution analogue to the nc82 label of Bruchpilot (Brp), a synaptic protein [19]. Synapse prediction reveals high-level neuropil structure not always evident from inspection of lower magnification EM data. Synapse prediction from EM data offers moreover advantages over nc82 immunolabeled data, because the accuracy of synapse density across neuropil regions can be verified by inspecting the high resolution EM data.

Our primary contribution lies in using synapse point clouds to instantly identify the boundaries of a neuropil in EM with great accuracy. This contribution leads to three applications:

1. Defining accurately regions of interest (ROIs). Having accurate ROIs is crucial to reconstruct connectomes because an imprecisely defined ROI

leads either to unnecessary, costly manual effort or an incomplete result.

2. Registration of EM synapse point cloud to light microscopy (LM) data to facilitate neuropil identification and exploit information annotated in the LM datasets especially in standard brain atlases [9].
3. Verifiable statistics of synapse packing density across different brain regions not limited to the outputs of particular cell types as in [14].

To test our methods, we have studied the organization and synapse density of the *Drosophila* antennal lobe (AL). Several light microscopic have previously classified the glomeruli [11, 13, 3, 5], neuropil compartments, in the AL, but the exact number has been uncertain. Glomeruli vary greatly in size depending on sex, sub-species, experience, and so on. This variation has confounded efforts to demarcate and classify the glomeruli precisely. While ideal comparisons control for genotype, experience level, etc, the size, shape, and locations of glomeruli can vary greatly and non-uniformly between *in vivo* and *in vitro* preparations, as a result of shrinkage and other disruptions from dissection [5]. Inspection of the EM data alone is insufficient to discern the boundaries between neighboring glomeruli (Figure 2). While the glia on the boundaries are often visible, it is often difficult to untangle these accurately from the rest of the neuropil, and as a result their locations fail to arbitrate the borders between glomeruli.

By contrast, application of our synapse prediction in the AL provides synapse point clouds of around 500,000 points that clearly reveal neuropil boundaries. We show how these clear boundaries lead to precise ROIs that could significantly reduce manual annotation effort. Furthermore, we successfully clustered this point cloud and were able to classify prominent glomeruli consistent with LM data. A reasonable registration between LM and EM synapse point clouds in such a variable neuropil provides some evidence that these techniques will generalize to other regions in the *Drosophila* brain. Finally, we extract synapse counts in different glomeruli that have been statistically validated by manually consulting the source EM data. Initial findings are compared against those from the previous literature and suggest potential additional analyses.

Specific contributions in this paper include:

1. Application of synapse predictions over a large region with a small amount of training data. The quality of these predictions suggests that object classification can be generalized across a large brain compartment.
2. Methods to efficiently define a region of interest using the synapse point cloud.
3. Clustering strategies that aid in the identification of AL glomeruli.
4. Visualization techniques for point cloud data that allow these to be registered with data from light microscopy.

We will first introduce our new methods. Then we will show results from applying synapse prediction to the AL, where this information is used to identify

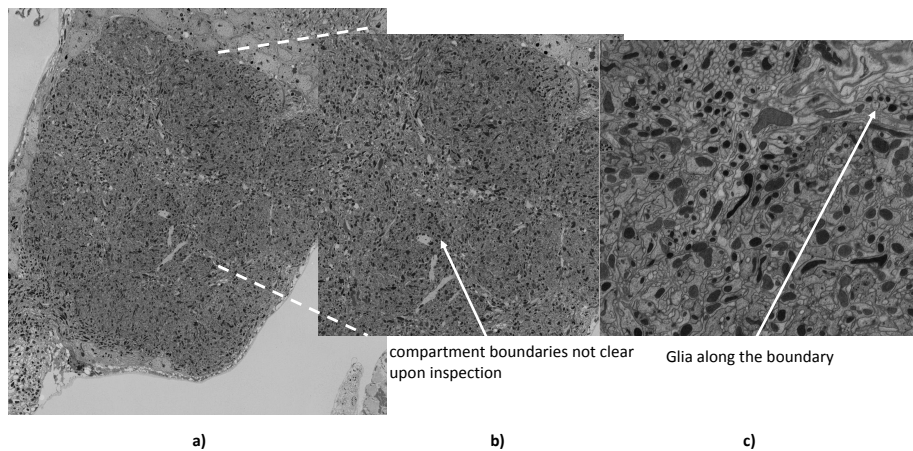


Figure 2: **Precise neuropil boundaries are difficult to discern from EM data alone.** a) The antennal lobe reveals some subtle differences in neuropil regions at lower magnification. b) With enlarged magnification, some of the boundaries become evident, while others remain unclear. c) Closer inspection reveals glia that help define the boundaries between glomeruli.

neuropil compartments and help define a ROI to better concentrate proofreading efforts. We conclude by discussing applications of these methods.

2 Methods

Figure 3 provides an overview of the methods introduced in this paper and the applications of those methods. In particular, it highlights our strategy for exploiting scalable, automatic synapse prediction.

We use images acquired by FIB-SEM techniques [10] to produce a large isotropic dataset. The isotropic resolution improves image alignment and, generally, the effectiveness of machine learning algorithms [17], which is critical when analyzing very large datasets [15]. We then produce synapse predictions following the procedure outlined in [8]. To apply this approach to a very large dataset, both the training required for the classifier and the prediction algorithm must scale to handle very large datasets. Fortunately, the approach in [8] has shown itself to be effective with only a small amount of training. We later show results in which the prediction generalizes over the entire antennal lobe in *Drosophila*. However, in practice, one might need to generate training for each distinct neuropil region. The main computational bottleneck in [8] lies in computing the probability that each voxel belongs to a synapse. This step is distributed across a compute cluster with each local worker processing a small spatial subvolume of the entire region.

The application of synapse prediction produces a *synapse point cloud*. Unlike

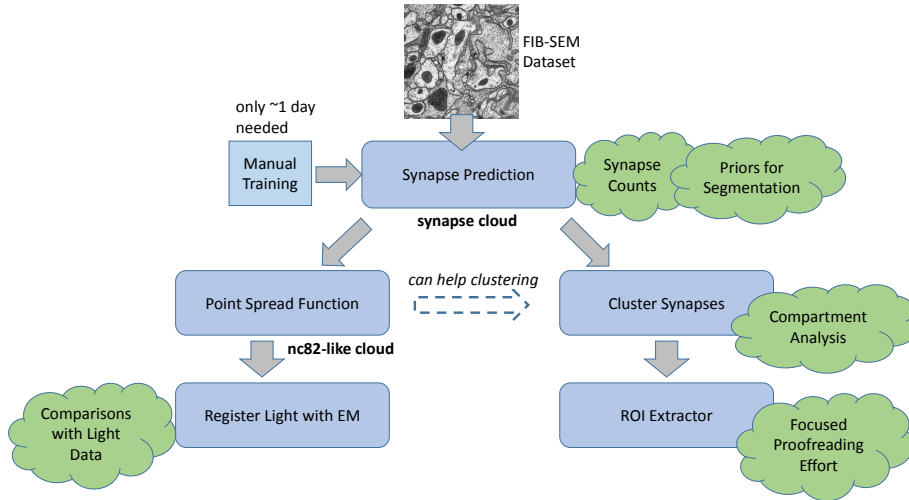


Figure 3: **ROI and Synapse Methodology.** The light blue boxes show the parts of our methods. The green clouds indicate potential applications explored in this paper.

algorithms that automatically extract neuron shapes from EM, in which small automatic errors can exert considerable impact on the connectome [17], we conjecture that small inaccuracies in the synapse point cloud will have only a minimal effect on our ability to analyze high-level trends. Given the resolution of EM data, these predictions can be sampled and accurate synapse counts for different regions can be provided, which is generally difficult using nc82 immunolabeling. We also suggest the potential for using these predictions as hints for image segmentation algorithms.

Synapse Density Maps. We apply a Gaussian point spread function (PSF) to the synapse point cloud to generate a smooth map of synapse density. If the synapse cloud contains N points and the center of the i th point is \mathbf{c}_i , the density map is defined as:

$$D(\mathbf{x}) = t \sum_{i=1}^N e^{-\frac{(\mathbf{x}-\mathbf{c}_i)^2}{2}} \quad (1)$$

where \mathbf{x} is a point in the 3D space and t is the normalization factor, which scales the density to cover the full value range for an image of a given bit depth.

The density map has several applications. For example, the density map resembles the lower resolution data from nc82 light microscopy. Given this, we can register light and EM datasets from similar neuropil regions using the techniques introduced in [1]. Because nc82 and EM preparations are different, there will be neuropil variations. Despite these variations, our results show that we are still able to register prominent neuropil landmarks. Such registration

could guide neuronal tracing in EM data by using high-level information from light microscopy, although we do not pursue that application in this paper.

The density map also allows us to cluster the image into different neuropil regions through image segmentation. This is done by resampling the map to produce a 3D digital image that can be directly fed into any image segmentation method. We perform segmentation using a semi-automated approach. While clustering with unsupervised approaches like hierarchical-based clustering is sometimes possible when applied directly on a synapse point cloud, we achieved a better clustering result by manually adding seeds to disjoint compartments visible in the density map. Seeded watershed [2] is then applied on the density map to achieve the final clustering (thus avoiding the need to laboriously outline the exact boundaries in three dimensions). In many cases, subtle changes and discontinuities in the point cloud are picked up by the automated algorithms, allowing one to see compartment boundaries clearly. This information can be used to define neuropil regions, as we show later for the antennal lobe.

To obtain good segmentation results, the Gaussian PSF should reveal the gaps between the compartments while making each compartment as smooth as possible. According to the light microscope data, the minimal gap size between neighboring compartments is about $2\mu m$, which means the maximal value of σ should be similar. In our implementation, density map resampling resulted in a 3D image with the voxel size $0.16\mu m$ along each dimension, which means $\sigma \leq 12.5$ in pixel units. We tested two values $\sigma = 5$ and $\sigma = 10$ and found that $\sigma = 10$ performed better for the seeded watershed algorithm used.

Defining ROIs with Point Clouds. These neuropil clusters can be invaluable for defining ROIs for EM proofreading and used to validate previous boundaries as determined by LM data. For instance, it is often desirable to answer questions like: What are all of the connections within a specific brain compartment? We therefore need ways to annotate which portions in the neuropil are in this region and which not. Because the compartments cannot be precisely defined by a simple bounding box, in general, we need a different approach to define the region. To this end, we introduce a set of algorithms (described below) in the package Neutu [20] and DVID [21].

DVID defines an ROI at the granularity of small blocks ($32 \times 32 \times 32$ pixels). Each ROI consists of a list of coordinates to these blocks. In this manner, we can more concisely define an arbitrary region with only a small sacrifice in precision. The tool Neutu enables users to quickly define an ROI by drawing *loops* in different image planes. The user can draw the loop as a series of line segments that will snap to the contours, as shown in Figure 4a. The contour is chosen as a shortest path through the grayscale data between the two endpoints of the line segment. The user does not have to draw the ROI completely. Neutu will interpolate between loops drawn on non-consecutive planes. Using this approach, we can precisely and quickly define neuropils. An ROI encompassing the entire AL was quickly produced and is shown in Figure 4b.

As we saw in Figure 2, it is often hard to determine the boundary of the neuropil from the EM data alone. The synapse clusters provide hints for defining

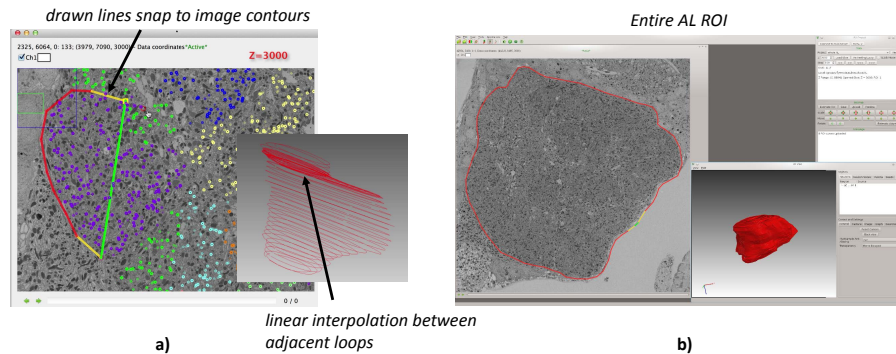


Figure 4: **Extracting an ROI from an EM dataset.** a) Tracing algorithm implemented in Neutu allows a proofreader to select a large region efficiently using clustered synapse predictions as a guide. b) Shows the ROI for the entire AL (around $300 \cdot 10^3 \mu\text{m}^3$).

compartment boundaries. In Section 3.4, we show how precise definition of the region produces significant reduction of manual EM proofreading effort, the primary bottleneck to scaling connectome reconstruction.

3 Empirical Evaluation

To test our methodology, we analyzed a dataset containing the AL of the 3-day old adult, female *Drosophila melanogaster*. The sample was prepared from a $250\mu\text{m}$ frontal head slice of a fly obtained by crossing homozygous w1118 with CS wild type, prefixed for 20 min in 2.5% each of paraformaldehyde and glutaraldehyde in 0.1 cacodylate buffer, then high-pressure frozen and freeze substituted in 1% OsO₄ and 0.2% uranyl acetate. A volume roughly containing the entire AL was imaged from 2nm milling depths using FIB and 8nm resolution using SEM. For consecutive image planes were averaged to yield 8nm resolution in the z-axis. Alignment was then performed on the dataset to produce a 3D image stack with 8x8x8 nm resolution.

3.1 Synapse Prediction

To predict synapses in the AL, we first manually annotated a subvolume of the AL roughly encompassing one glomerulus. This region was split into training and validation, in order to train a classifier for automatic T-bar detection, and to set the threshold for the classifier to yield approximately 0.9 recall (*i.e.*, so that 90% of real T-bars were found) corresponding to a precision of 0.8 (*i.e.*, 80% of the T-bars found were correct) on the validation data.

In our implementation, we made use of a shared cluster resource in which up

to 2500 cores were available (with variations depending on load from other users). The trained classifier was then applied to the entire AL, which was about 680 gigavoxels in size. Inference over this full volume took 11 days, and produced approximately $520 \cdot 10^3$ T-bar detections.

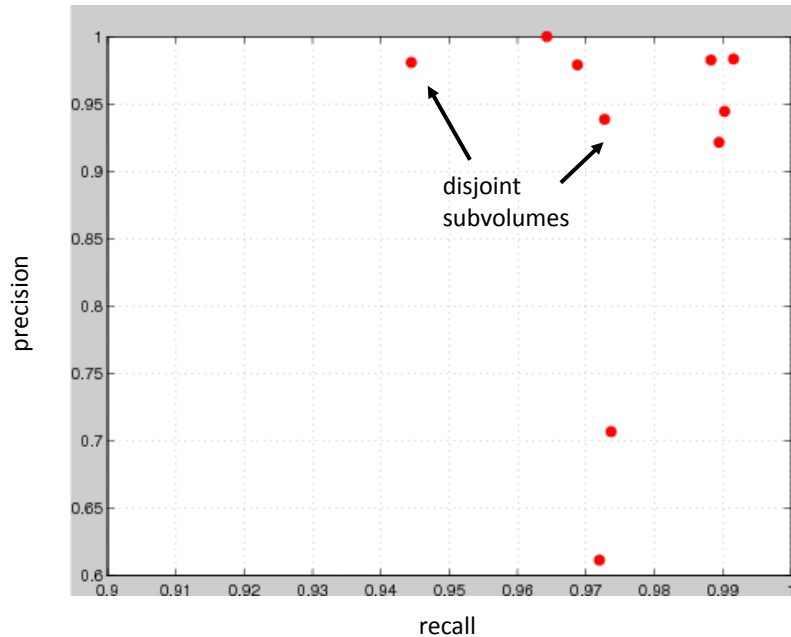


Figure 5: **Generalizability of the synapse classifier over the AL.** Automated T-bar predictions within 10 randomly chosen subvolumes were manually inspected. The precision and recall is over 90 percent for most subvolumes. There are two subvolumes with lower precision (< 0.9).

To assess how well the classifier generalized across the entire image region, predictions within a small number of randomly selected subvolumes, spread across the whole ROI, were manually reviewed. Figure 5 indicates precision and recall are over 90% for most subvolumes. However, some outliers exist, which are a result of darker regions in the image volume, as shown in Figure 6. For example, dark granules in a soma result in several mis-predictions. A negative result is not surprising since the somata exist at the periphery of the neuropil in the fly brain and were not included in our training dataset.

These generalization errors can potentially be resolved using multiple approaches. One simple technique is to locally normalize each subvolume, such that the subvolume has 0 mean and unit standard deviation, as a means of compensating for regions where the image has darker intensity. As shown in Figure 7, the low precision outlier substacks are significantly improved by this normalization, with only a slight average degradation to the rest of the samples.

Alternatively, additional training samples could be collected from regions where the original classifier performed poorly, and used to either re-train the classifier, or train a new classifier specific to regions where the original classifier did not generalize well.

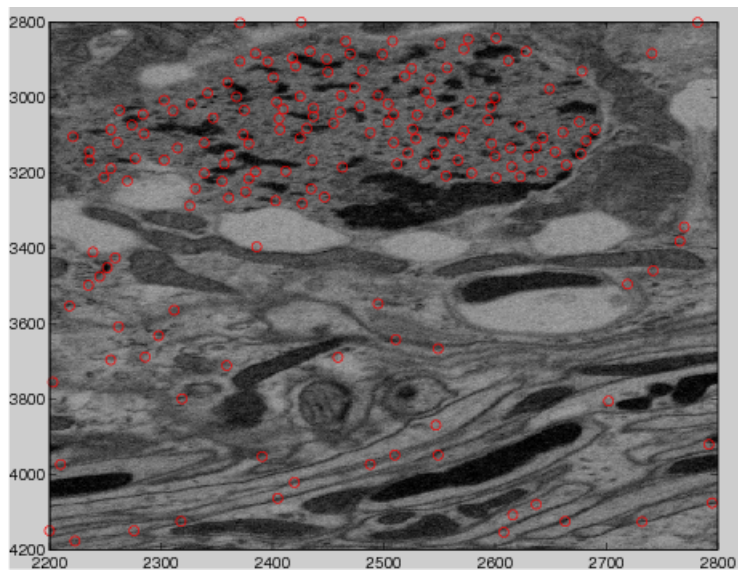


Figure 6: **Examples of neuropil with over-prediction.** Dark granules in neuronal soma caused several false positives in the predictor. Normalizing the image contrast improves the quality of the prediction.

While the previous analyses show a good overall prediction accuracy and that the variance in accuracy between random regions is reasonably consistent, subtle biases between regions could undermine particular analyses. We will explore this shortly in the context of estimating the synaptic density across the AL glomeruli.

3.2 Synapse Cloud and Registration

We showed that synapse prediction can be done with a small amount of training in a manner that generalizes well statistically across the entire AL. As a subsequent evaluation of the robustness of our result, we compared it against preparations in which nc82 antibody was used to label the Brp protein at pre-synaptic T-bars.

Figure 8a shows a synapse cloud containing over 500,000 synaptic points. After applying a Gaussian point spread function over the data in Figure 8b we can discern some of the AL compartments, noting qualitative similarities to confocal images of an nc82 dataset. Because of differences in the protocols used to prepare images between our sample and the nc82 dataset, we expect variation in glomeruli size and shape. While the inability to register the two datasets would not necessarily invalidate our techniques, it is significant that even a rough

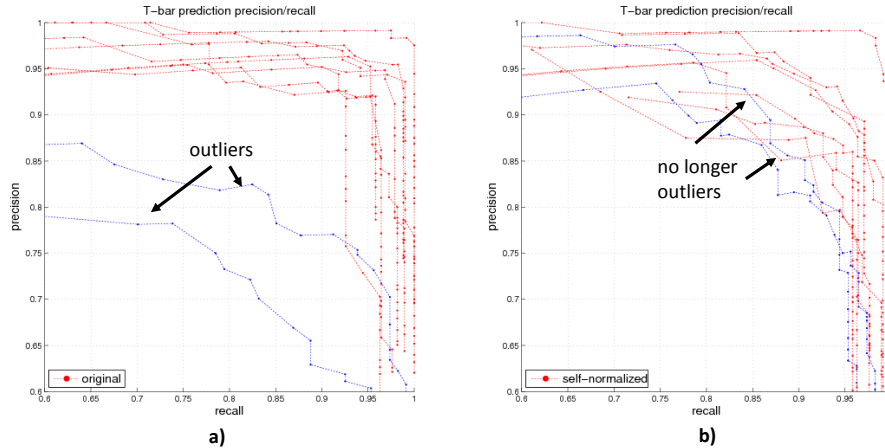


Figure 7: **Improved consistency in prediction after normalization.** a) The precision and recall over 10 subvolumes without normalization leads to two outliers. b) These outliers are removed when normalizing each subvolume to 0 mean and unit standard deviation.

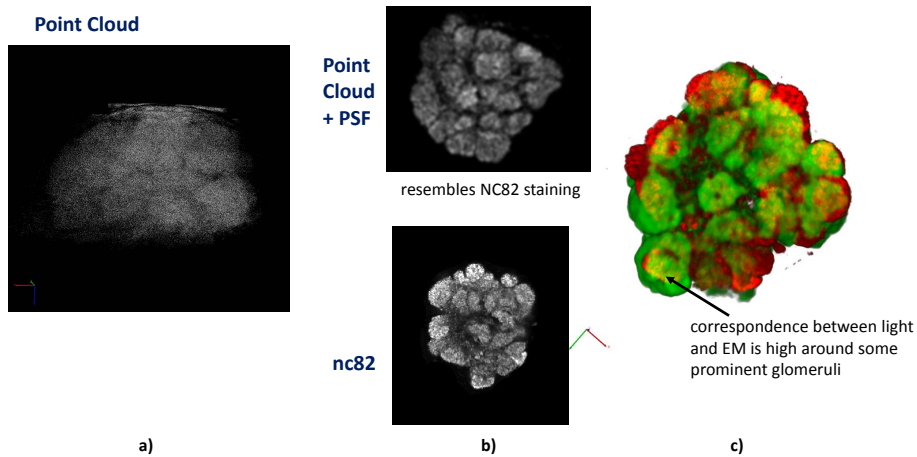


Figure 8: **From synapse point cloud to EM/light registration.** a) Synapse cloud contains over 500,000 synaptic points. It is difficult to determine the biological compartments. b) A Gaussian point-spread function is applied producing data that looks similar to nc82 immuno-images, revealing glomeruli compartments in the AL. c) Registration of EM and LM volumes shows good correspondence for some of the more prominent compartments.

registration was possible, as shown in 8c, suggesting the biological relevance of our EM and machine learning approach to the problem. Note that some of the prominent glomeruli regions are common in both datasets.

3.3 Application 1: Defining Glomeruli and Analyzing Synapse Density in the AL

Figure 9 shows the result of semi-automatic clustering of the synapse point cloud followed by some manual revision of the clusters. We identify 49 compartments, close to the 54 identified in a previous study [5]. As noted, the exact number and size of AL glomeruli are both difficult to characterize definitively. This is due in part to intraspecies variability and sensitivity to image preparation procedures. We do not aim to clarify this situation. Instead, we focus on whether the synapse point cloud can be used to define glomerular boundaries in general. Figure 9 shows labels for some of the more prominent glomeruli. The proper registration of this dataset to a standard brain derived from nc82 samples makes the task of labeling more straightforward. Notice that several prominent glomeruli are clearly identified. The feasibility of this task confirms that synapse clouds can be used for such analysis.

We also consider whether automatic synapse prediction permits analysis of variations of synaptic density across glomeruli. Making a strong claim about synaptic variation in the presence of approximate synapse prediction across glomeruli with ambiguous boundaries may not be possible. Also, comparing synaptic density between our sample and others is further complicated by the non-uniform shrinkage that occurs in the AL due to image preparation [5]. To improve the analysis, we restrict our attention to glomeruli with boundaries and in which the correspondence to previous literature is strongest. Future work could entail generating predictions over multiple EM datasets, which would greatly improve the robustness of our result.

Table 1 show the size and synapse density for all compartments of the AL. The labeled glomeruli are indicated with appropriate names. The high variation in glomerular size corroborates previous anatomical studies from LM. The density differences are more interesting. Synapse density range from under 2 per cubic micron to over 3 per cubic micron. An overall density of 2.4 synapses per cubic micron is predicted (perhaps slightly more in practice depending on the recall as discussed in the next paragraph). Do these density variations reflect reality or are they the outcome of expected variation in the prediction, along with non-uniform size changes of the glomeruli that result from image preparation?

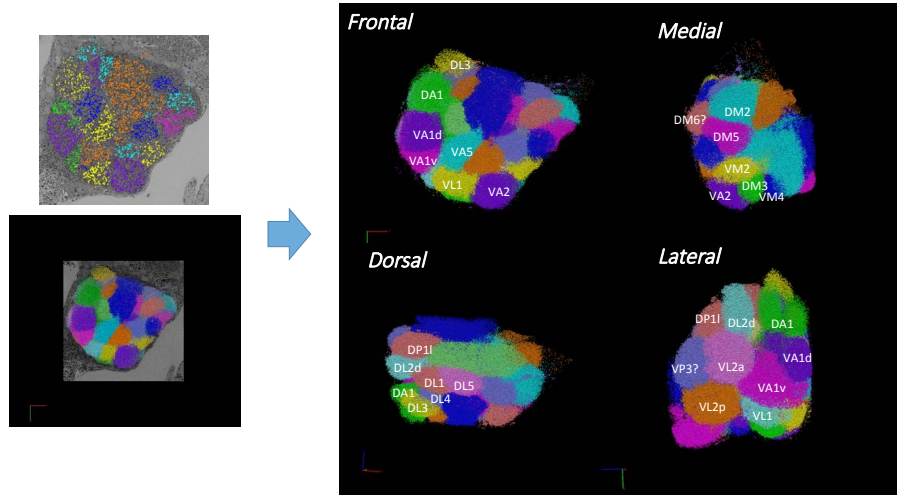


Figure 9: **Semi-automatic synapse cloud clustering and identification of several glomeruli.** Around 60 regions are first conservatively segmented using the synapse point cloud and seeded watershed with manually placed seeds. The clusters are then manually refined to produce 50 regions. 26 of these regions are given names consistent with those previously reported in the literature.

Table 1: **Density of predicted synapses in different segmented compartments.** The density of synapses range from 1.5 to 3.3 synapse per cubic micron. The target glomerulus for manual annotation was VA1v. The last column adjusts the synapse density based on manual spot checking.

glomerulus	#synapses	cubic microns	#synapses/ cubic microns	adjusted
unlabeled	804	526	1.53	unchecked
unlabeled	1002	546	1.84	unchecked
unlabeled	1676	748	2.24	unchecked
unlabeled	2031	955	2.13	unchecked
DA3?	2230	976	2.28	unchecked
unlabeled	1816	1012	1.79	unchecked
VL1	9792	3614.04	2.71	unchecked
unlabeled	5111	1645	3.11	unchecked
unlabeled	2641	1655	1.60	unchecked
DL3	2984	1694	1.76	unchecked
unlabeled	3796	1872	2.03	unchecked
unlabeled	4448	1872	2.38	unchecked
VA4	5068	2006	2.53	unchecked

Continued on next page

Table 1 – continued from previous page

glomerulus	#synapses	cubic microns	#synapses/ cubic microns	adjusted
VM3	5232	2202	2.38	unchecked
unlabeled	5904	2388	2.47	unchecked
DM3	7615	2646	2.88	unchecked
unlabeled	6159	2648	2.33	2.64
VM2	5814	2659	2.19	unchecked
unlabeled	6740	2763	2.44	unchecked
unlabeled	6341	2770	2.29	2.50
unlabeled	9969	3004	3.32	2.77
DL5?	8851	3174	2.79	unchecked
unlabeled	6322	3181	1.99	unchecked
DM6	7704	3245	2.37	unchecked
VA3?	9224	3461	2.67	unchecked
DL1	10165	3541	2.87	unchecked
unlabeled	8031	3712	2.16	unchecked
DM5	8856	3995	2.22	2.69
unlabeled	11100	4107	2.70	unchecked
unlabeled	9443	4215	2.24	2.60
unlabeled	9683	4335	2.23	unchecked
unlabeled	8966	4395	2.04	unchecked
VP3?	12002	4508	2.66	unchecked
unlabeled	13607	5162	2.64	2.59
VA2	13548	5399	2.51	3.01
VA1d	11669	5652	2.06	unchecked
DA1	8778	5803	1.51	4.18
VA5?	18009	5826	3.09	unchecked
VL2a	16323	5987	2.73	3.15
DP1L	18369	6066	3.03	unchecked
DM2	15729	6714	2.34	unchecked
DL2d	18651	6719	2.78	unchecked
VL2p	17370	6720	2.58	unchecked
VA1v	16513	7021	2.35	2.20
V	20132	7257	2.77	unchecked
unlabeled	20743	7364	2.82	unchecked
unlabeled	22767	9452	2.41	unchecked
unlabeled	30951	16855	1.84	unchecked
VM4	49165	25510	1.93	unchecked
totals	519844	219577	2.4	-

We first aim to better understand the variation that results from predictor inaccuracy. While Figure 5 shows consistency and generalizability of the predictor, through manual verification of predictions in randomly sampled regions, bias

is still possible. For example, one glomerulus could have different contrast or neuropil structures than other glomeruli, confounding comparisons between different glomeruli. To test for this possibility, we manually identified synapse annotations for 10 small subvolumes ($64 \mu\text{m}^3$ in size) in the center of distinct, well-defined glomeruli that exhibit varying synaptic densities. The hope was to observe consistent precision / recall. The results in Table 2 show that predictions over most subvolumes find 70 - 90% of real synapses (recall) and that 70 - 90% of all predictions are real synapses (precision). However, two substacks (shown in bold) are significant outliers. The low precision for the second subvolume appears to be the result of a dark image as discussed previously. *DA1* misses several synapses. This appears to result from a very low-contrast image. We use these precision / recall numbers to update the corresponding synapse density estimate in Table 1. While the variation, even among the regions with more consistent prediction, is too large to make definitive claims, a preponderance of glomeruli with 2.2 to 2.8 synapses per μm^3 is evident. Interestingly, the manually examined subvolumes contain significant variance in identified synapses, but insofar as the subvolumes are only approximately in the center of each glomerulus, the variation may result from differences within a glomerulus. It may also reflect non-uniform volume differences in the AL.

Table 2: **Accuracy of predictor compared to 10 subvolumes in the center of 10 different glomeruli.** The predictor performs similarly for all but two of the substacks highlighted below.

glomerulus	recall	prec
unlabeled	0.78	0.85
unlabeled	0.81	0.68
DM5	0.73	0.88
VA2	0.70	0.84
VL2a	0.70	0.81
unlabeled	0.77	0.89
VA1v	0.88	0.82
DA1	0.29	0.79
unlabeled	0.88	0.86
unlabeled	0.79	0.89

In future work, we will try to better understand the density of the synapses across glomeruli compared with those previously reported by normalizing our data to glomeruli sizes in published *in vivo* studies. This will reduce the impact of distortion caused by image preparation and enable more accurate comparisons of synapse counts.

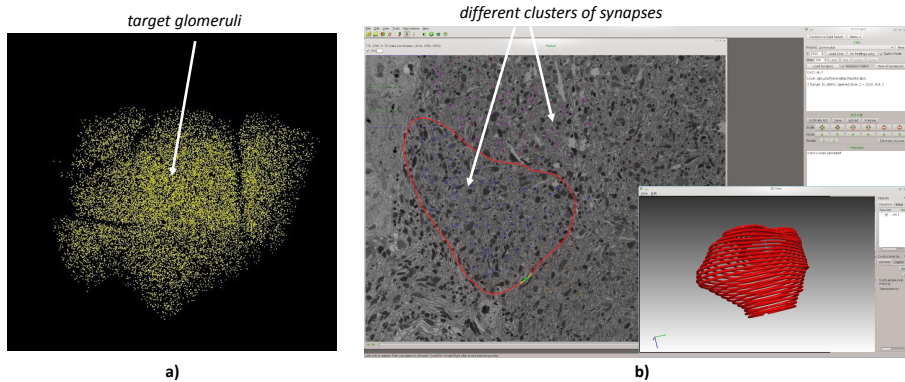


Figure 10: **Determining Region of Interest to help focus proofreading efforts using synaptic information** . a) Manually identified synapses in AL show that some synapses go beyond the target glomeruli (VA1v). b) Using these annotations, a specific ROI was determined using the tool NeuTu.

3.4 Application 2: Reducing EM Proofreading Effort by Selecting the Region of Interest

We now show how synapse clouds can reduce proofreading work. We originally tried to analyze the connectome within a glomerulus. To determine the connectome, we first annotated all of the synapses in a region believed to contain an entire glomeruli. The initial boundary was based on what appeared to be glia and was known to be an approximation. It was unclear how accurately located this initial ROI would be until we started annotating the synapses.

A total of 19921 synapses were manually annotated taking a little over 38 8-hour proofreader days to complete. These annotations were used as training for the synapse prediction but also indicated the boundaries with adjacent glomeruli, as shown in Figure 10.a. These synapses were clustered into different regions. By showing the pattern of their clusterings and grayscale in NeuTu, we asked an expert to define more precisely the glomerulus boundary by drawing loops through the low-density synapse regions.

The resulting glomerulus ROI, identified to be a large portion of VA1v, is $4858 \text{ } \mu\text{m}^3$ compared with $11875 \text{ } \mu\text{m}^3$ of the original region manually annotated (the entire AL is over $285000 \text{ } \mu\text{m}^3$). Only 11256 synapses were actually located in glomerulus ROI. If this ROI had been chosen before performing any manual annotation, there would have been roughly a 43% reduction in the work/annotation. Subsequent tracing and connectome analysis can also be better defined with this ROI. Note that the synapses per cubic micron manually annotated was 2.31, close to the 2.35 listed for VL1 in Table 1. Note that the manually annotated and drawn ROI is actually still a subset of the whole VL1; a subset of the manual annotation was used to train the predictor.)

Our experiments also show that defining an ROI in NeuTu by manually

drawing several 2D loops is time-efficient. The glomerulus ROI and entire AL ROI required 45 and 84 loops respectively and took under a day to trace.

4 Discussion

We show that automatic analysis of large EM datasets, such as uncovering different neuropil compartments, counting synapses, and estimating their packing density, is possible using fully automatic if imperfect synapse prediction protocols. Sampling our predictions gives us confidence that synapse counts are statistically accurate.

We believe automatic synapse prediction could also be useful in guiding image segmentation and reducing manual effort in connectome reconstruction. For instance, eliminating manual synapse annotation in connectome reconstruction will significantly reduce labor - the manual effort required to annotate the entire AL dataset alone would require 1,000 proofreader days. Fortunately, in many cases and for many applications inaccuracy in the prediction of synaptic sites might not harm downstream connectome analysis. First, many pathways have redundant connections. Also, note that in a previous report, the consistency between manual annotators is only around 90%, not much better than with our automatic approach [16]. (This consistency could also be further improved with more time-consuming, double-checking and consensus-based proofreading but for identification and characterization of strong pathways, this would not in fact be required.) Ultimately, using automatic synapse prediction in a connectome will require more detailed analysis to ensure that subtle biases are not introduced.

We introduce synapse density statistics for the AL and several constituent glomeruli. We enlist the superior resolution of EM data to make claims about the accuracy of our approach. While small inaccuracies in the synapse prediction currently prevent conclusive claims for differences in synaptic density between glomeruli, both our manual annotation and predictions suggest that a synapse packing density exists that is far greater than previously reported using the construct Brp-short [14]. The authors of this previous report [14] reveal a consistent packing density of olfactory receptor neuron outputs across several glomeruli in a 10-day adult *Drosophila*. It is possible that Brp-short does not label all synapses, just as nc82 at a dilution used labels only a fraction of the T-bar ribbons in the optic lamina [6]. The differences in synaptic counts could also be from AL interneurons or projection neurons. However, specimen differences complicate this comparison (for instance degeneration at synapses could already be present). Future work could strengthen the analysis by generating predictions from multiple samples. In addition, ongoing semi-automatic reconstruction efforts in the AL will eventually reveal the exact distributions of connections per neuron class.

We note that our synapse clouds are closely related to nc82 immunopuncta or other synapse labeled data. For some analyses, EM synapse point clouds are a preferred alternative, for example when synapse point labels require verification or when subclasses of synapses need to be analyzed. Another consideration is the

unknown effectiveness of nc82 in detecting synapses with different compositions and maturities. Brp is localized to the platform of the T-bar [4]. In some EM data, we note that the platforms are not fully developed. It is unclear how these T-bars will be labeled in an nc82 sample, whereas, a more detailed analysis could be undertaken in the EM data. Anecdotally, we observe that our synapse cloud contains these partial synapse sites.

The biggest obstacle to high-throughput generation of EM synapse point clouds is the speed of image acquisition. Synapse prediction requires minimal training and can be computed quickly on a cluster. Continual advances in imaging technology promise to reduce acquisition bottlenecks greatly.

References

- [1] Y. Aso, D. Hattori, Y. Yu, R. Johnston, N. Iyer, T. Ngo, H. Dionne, L. Abbott, R. Axel, H. Tanimoto, G. Rubin, "The neuronal architecture of the mushroom body provides a logic for associative learning," *eLife* 2014, doi:10.7554/eLife.04577
- [2] S. Beucher, F. Meyer, "The morphological approach to segmentation : the watershed transformation," *Mathematical Morphology in Image Processing* 1993, pp. 433-481.
- [3] A. Couto, M. Alenius, B. Dickson, "Molecular, anatomical, and functional organization of the *Drosophila* olfactory system," *Current Biology* 2005, pp. 1535-1547.
- [4] W. Fouquet, D. Oswald, C. Wichmann, S. Mertel, H. Depner, M. Dyba, S. Hallermann, R. Kittel, S. Eimer, S. Sigrist, "Maturation of active zone assembly by *Drosophila* Bruchpilot," *J Cell Biol.*, 2009, 186(1):129-145.
- [5] V. Grabe, A. Strutz, A. Baschwitz, B. Hansson, S. Sachse, "Digital in vivo 3D atlas of the antennal lobe of *Drosophila melanogaster*," *Journal of Comparative Neurology* 2014, doi: 10.1002/cne.23697.
- [6] Y. Hamanaka, I. Meinertzhagen, "Immunocytochemical localization of synaptic proteins to photoreceptor synapses of *Drosophila melanogaster*," *J. Comp. Neurol.* 2010, 518, pp. 1133-1155.
- [7] M. Helmstaedter, K. Briggman, S. Turaga, V. Jain, H. Seung, W. Denk, "Connectomic reconstruction of the inner plexiform layer in the mouse retina," *Nature* 2014, pp. 168-174.
- [8] G. Huang, S. Plaza, "Identifying synapses using deep and wide multiscale recursive networks," *ArXiv*, September 2014.
- [9] A. Jennet, *et. al.*, "A GAL4-driver line resource for *Drosophila* neurobiology," *Cell Reports*, 2012, doi:10.1016/j.celrep.2012.09.011.

- [10] G. Knott, H. Marchman, D. Wall, B. Lich, “Serial section scanning electron microscopy of adult brain tissue using focused ion beam milling,” *J. Neurosci*, 2008, pp. 2959-2964.
- [11] Y. Kondoh, K. Kaneshiro, K. Kimura, D. Yamamoto, “Evolution of sexual dimorphism in the olfactory brain of Hawaiian *Drosophila*”, *Proc. R. Soc. Lond.*, 2003, pp. 1005-1013.
- [12] A. Kreshuk, C. Straehle, C. Sommer, U. Koethe, M. Cantoni, G. Knott, F. Hamprecht, “Automated detection and segmentation of synaptic contacts in nearly isotropic serial electron microscopy images,” *PLOS ONE*, 2011, doi: 10.1371/journal.pone.0024899.
- [13] P. Laissue, C. Reiter, P. Hiesinger, S. Halter, K. Fischbach, R. Stocker, “Three-dimensional reconstruction of the antennal lobe in *Drosophila melanogaster*,” *Journal of Comparative Neurology* 1999, pp. 543-552.
- [14] T. Mosca, L. Luo, “Synaptic organization of the *Drosophila* antennal lobe and its regulation by the Teneurins,” *eLife* 2014, doi: 10.7554/eLife.03726. n
- [15] S. Plaza, L. Scheffer, D. Chklovskii, “Toward Large-Scale Connectome Reconstructions,” *Current Opinion in Neurobiology*, April 2014, pp. 201-210.
- [16] S. Plaza, “Annotating synapses in large EM datasets,” *ArXiv*, rev. December 2014.
- [17] S. Plaza, “Focused proofreading: efficiently extracting connectomes from segmented EM images,” *ArXiv*, September 2014.
- [18] O. Trujillo-Cenóz, “Some aspects of the structural organization of the medulla in muscoid flies,” *J. Ultrastruct. Res.*, 1969, 27:533-553.
- [19] D. Wagh, T. Rasse, E. Asan, A. Hofbauer, I. Schwenkert, H. Drrbeck, S. Buchner, M. Dabauvalle, M. Schmidt, G. Qin, C. Wichmann, R. Kittel, S. Sigrist, E. Buchner, “Bruchpilot, a protein with homology to ELKS/CAST, is required for structural integrity and function of synaptic active zones in *Drosophila*,” *Neuron*, 2006, Mar 16;49(6):833-44.
- [20] NeuTu: Software package for neuron reconstruction and visualization. <https://github.com/janelia-flyem/NeuTu>
- [21] DVID: Distributed, versioned, image-oriented datastore. <https://github.com/janelia-flyem/dvid>
- [22] S. Takemura, A. Bharioke, Z. Lu, A. Nern, S. Vitaladevuni, *et al*, “A visual motion detection circuit suggested by *Drosophila* connectomics,” *Nature*, 2013, pp. 175-181.

Acknowledgements: We thank Zhiyuan Lu for sample preparation; Shan Xu and Harald Hess for FIB-SEM imaging; the FlyEM proofreading team (Lei-Ann Chang and the Dalhousie proofreading team) for the annotations efforts; and Yang Yu for EM/light registration.